

Supplementary Material: Megapixel Adaptive Optics

CONGLI WANG, QIANG FU, XIONG DUN, and WOLFGANG HEIDRICH,

King Abdullah University of Science and Technology, Saudi Arabia

S.1 WAVEFRONT SOLVER DETAILS

Derivations

The linearized wavefront estimation problem in primary paper is:

$$\underset{\phi}{\text{minimize}} \quad \|\mathbf{GM}\nabla\phi + \mathbf{g}_t\|_2^2 + \beta \|\nabla\phi\|_2^2, \quad (\text{S.1})$$

recall that matrix $\mathbf{G} = [\text{diag}(\mathbf{g}_x) \text{diag}(\mathbf{g}_y)]$.

By introducing a slack variable \mathbf{w} , whose physical interpretation is the wavefront gradient, the original objective function in Eq. (S.1) can be split into two parts, as:

$$\begin{aligned} \underset{\phi, \mathbf{w}}{\text{minimize}} \quad & \underbrace{\|\mathbf{GM}\mathbf{w} + \mathbf{g}_t\|_2^2}_{g(\mathbf{w})} + \underbrace{\beta \|\nabla\phi\|_2^2}_{f(\phi)}, \\ \text{subject to} \quad & \mathbf{w} = \nabla\phi. \end{aligned} \quad (\text{S.2})$$

Using ADMM then it yields Algorithm S.1, where η is the dual variable, and a “warm starting” numerical strategy is employed to fasten convergence, i.e. initializing the solution for one frame with the solution from previous frame. Now we briefly discuss how the ϕ -update step and \mathbf{w} -update step are computed.

Algorithm S.1 ADMM for solving Eq. (S.1).

- 1: **procedure** RECONSTRUCT WAVEFRONT($\mathbf{g}_x, \mathbf{g}_y, \mathbf{g}_t$)
- 2: Initialize ϕ^0, \mathbf{w}^0 and η^0 from previous frame, set $\mu > 0$;
- 3: **while** not converge **do**
- 4: $\phi^{k+1} \leftarrow \arg \min_{\phi} f(\phi) + \mu \|\nabla\phi - \mathbf{w}^k + \eta^k\|_2^2$;
- 5: $\mathbf{w}^{k+1} \leftarrow \text{prox}_{g/\mu}(\nabla\phi^{k+1} + \eta^k)$;
- 6: $\eta^{k+1} \leftarrow \eta^k + \nabla\phi^{k+1} - \mathbf{w}^{k+1}$;
- 7: **end while**
- 8: **end procedure**

ϕ -update step This involves solving a Poisson equation, which usually requires proper boundary conditions in conventional approaches, for example the periodic boundary condition [Hudgin 1977], or the Neumann boundary condition [Noll 1978]. However, in our case, because of the existence of \mathbf{M} , the unknown boundary values are implicitly determined by minimizing the objective. When trivial boundary conditions are assumed, the solution to the resultant Poisson equation leads to non-trivial boundary values on the observed part of ϕ . In practice, we found Neumann boundary condition suffices to yield a good estimation (see Figure S.1). Therefore, by

Permission to make digital or hard copies of part or all of this work for personal or classroom use is granted without fee provided that copies are not made or distributed for profit or commercial advantage and that copies bear this notice and the full citation on the first page. Copyrights for third-party components of this work must be honored. For all other uses, contact the owner/author(s).

© 2017 Copyright held by the owner/author(s).
0730-0301/2018/8-ART115

<https://doi.org/10.1145/3197517.3201299>

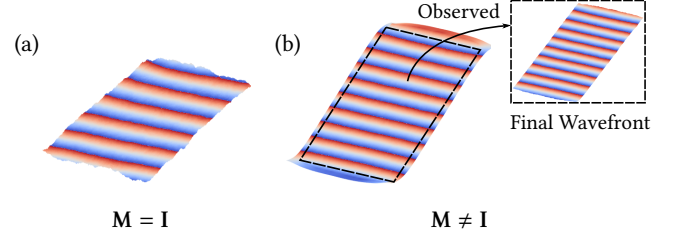


Fig. S.1. Constructing tilt wavefront via Algorithm S.1 respectively by (a) ignoring boundary issues (i.e. $\mathbf{M} = \mathbf{I}$, where \mathbf{I} is the identity matrix), and (b) using boundary matrix \mathbf{M} . In both cases, the reflective boundary conditions are assumed. Ignoring boundary effects yields additional tilting artifacts in the final reconstruction, whereas with boundary matrix \mathbf{M} the unobserved part of variable ϕ is recovered with sufficiently good values, and boundary artifact is greatly reduced.

just assuming Neumann boundary condition on the linear operators, denoting \mathcal{F}_{DCT} and $\mathcal{F}_{\text{DCT}}^{-1}$ as forward and inverse Discrete Cosine Transforms (DCT) respectively, the ϕ -update is given as:

$$\begin{aligned} \phi^{k+1} &= \arg \min_{\phi} \beta \|\nabla\phi\|_2^2 + \mu \|\nabla\phi - \mathbf{w}^k + \eta^k\|_2^2 \\ &= \left((\beta/\mu + 1) \nabla^2 \right)^{-1} \nabla^T (\mathbf{w}^k - \eta^k) \\ &= \mathcal{F}_{\text{DCT}}^{-1} \left(\frac{\mathcal{F}_{\text{DCT}} \left(\nabla^T (\mathbf{w}^k - \eta^k) \right)}{(\beta/\mu + 1) \mathcal{F}_{\text{DCT}} (\nabla^2)} \right), \end{aligned} \quad (\text{S.3})$$

where the division is element-wise. Note that forward/inverse DCT can be efficiently implemented via forward/inverse Fast Fourier Transforms (FFT), respectively.

\mathbf{w} -update step This involves evaluation of $\text{prox}_{g/\mu}(\mathbf{u})$, the proximal operator [Parikh et al. 2014] of $g(\mathbf{w})$ with parameter μ , which is defined and computed as:

$$\begin{aligned} \text{prox}_{g/\mu}(\mathbf{u}) &= \arg \min_{\mathbf{w}} \|\mathbf{GM}\mathbf{w} + \mathbf{g}_t\|_2^2 + \mu \|\mathbf{w} - \mathbf{u}\|_2^2 \\ &= (\mu \mathbf{I} + \mathbf{M}^T \mathbf{G}^T \mathbf{G} \mathbf{M})^{-1} (\mu \mathbf{u} - \mathbf{M}^T \mathbf{G}^T \mathbf{g}_t) \\ &= \mathbf{M}^T (\mu \mathbf{I} + \mathbf{G}^T \mathbf{G})^{-1} (\mu \mathbf{M} \mathbf{u} - \mathbf{G}^T \mathbf{g}_t) + (\mathbf{I} - \mathbf{M}^T \mathbf{M}) \mathbf{u}. \end{aligned} \quad (\text{S.4})$$

A closed form formula can be obtained for Eq. (S.4) because $\mu \mathbf{I} + \mathbf{G}^T \mathbf{G}$ is block-diagonal. Denote $\mathbf{u} = [\mathbf{u}_1^T \mathbf{u}_2^T]^T$, and use element-wise operator, then (notation: the arithmetic operators are element-wise):

$$\text{prox}_{g/\mu}(\mathbf{u}) = \begin{cases} \begin{bmatrix} \mathbf{u}_1^T & \mathbf{u}_2^T \end{bmatrix}^T, & \text{if } \mathbf{u} \text{ outside boundary,} \\ \begin{bmatrix} \frac{(\mathbf{g}_y^2 + \mu \mathbf{I}) \mathbf{u}_1 - \mathbf{g}_x \mathbf{g}_y \mathbf{u}_2 - \mathbf{g}_x \mathbf{g}_t}{\mathbf{g}_x^2 + \mathbf{g}_y^2 + \mu \mathbf{I}} \\ \frac{-\mathbf{g}_x \mathbf{g}_y \mathbf{u}_1 + (\mathbf{g}_x^2 + \mu \mathbf{I}) \mathbf{u}_2 - \mathbf{g}_y \mathbf{g}_t}{\mathbf{g}_x^2 + \mathbf{g}_y^2 + \mu \mathbf{I}} \end{bmatrix}, & \text{otherwise.} \end{cases}$$

Note that all the operations are either element-wise multiplications or divisions, and thus the computation of $\text{prox}_{g/\mu}(\mathbf{u})$ is highly efficient and is naturally parallelizable.

Comparison With Conjugate Gradient

In main text we compare our solver (Algorithm S.1) with conjugate gradient method that iteratively solves the unknown wavefront ϕ from the normal equation of Eq. (S.1):

$$\left(\nabla^T \mathbf{M}^T \mathbf{G}^T \mathbf{G} \mathbf{M} \nabla + \beta \nabla^2\right) \phi = -\nabla^T \mathbf{M}^T \mathbf{G}^T \mathbf{g}_t. \quad (\text{S.5})$$

Note the linear system cannot be diagonalizable either in spatial or frequency domain. To fasten convergence, a reasonable approach would be to first solve an unconstrained flow estimation problem:

$$\mathbf{w}^* = \arg \min_{\mathbf{w}} \|\mathbf{G} \mathbf{M} \mathbf{w} + \mathbf{g}_t\|_2^2 + \beta \|\mathbf{w}\|_2^2, \quad (\text{S.6})$$

and then integrate the gradient \mathbf{w}^* to serve as an initial guess to the conjugate gradient solver, as $\phi^0 = (\nabla^2)^{-1} \nabla^T \mathbf{w}^*$, assuming proper boundary condition. Using the previously introduced proximal operator notation, the solution can be written as $\mathbf{w}^* = \text{prox}_{g/\beta}(\mathbf{0})$, with $g(\mathbf{w})$ defined previously and $\mathbf{0}$ the null vector.

S.2 ADDITIONAL IMPLEMENTATION DETAILS

Timing

Figure S.2 shows that our GPU solver & controller runs in real-time with the camera sensor hardware synchronized to V-Sync, while the SLM is lacking the total speed because of its long response time. One whole AO iteration may probably take 5 or more V-Sync cycles, and hence reducing the total AO system performance to be only at around 10 Hz.

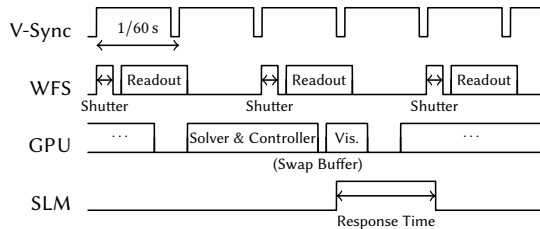


Fig. S.2. Example timing at one AO iteration (phase captured, reconstruction, and update).

Simulation

All parameters of the AO simulation in main text are listed in Table S.1. The generation of the turbulence wavefronts follows the subharmonics method [Lane et al. 1992], respecting Kolmogorov's law [Kolmogorov 1941]. Deformation functionality is mimic by bicubic interpolation.

Fabrication

The binary phase mask is fabricated on a 0.5 mm thick 4" Fused Silica wafer using photolithography techniques. We illustrate the fabrication pipeline in Figure S.3 and explain each step in details.

First, the designed binary phase (either 0 or π) is converted to a binary mask pattern (either 0 or 1 and written on a photomask

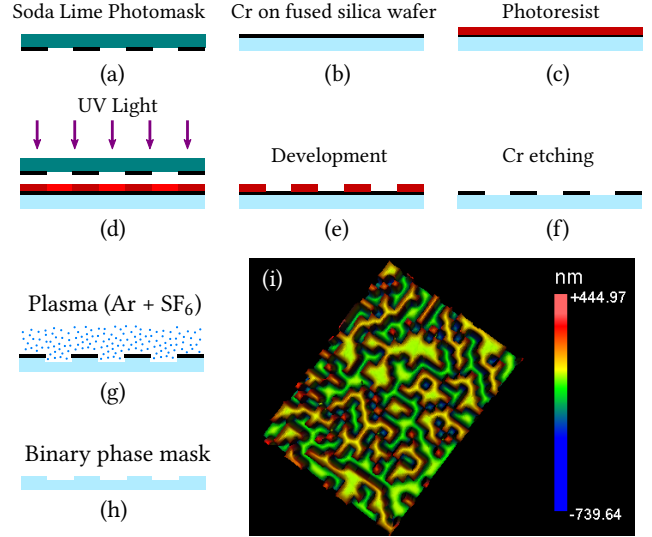


Fig. S.3. Fabrication of binary phase mask. (a) The designed mask patterns are first written on a Soda Lime photomask with laser direct writer. (b) A thin layer of Cr is deposited on one side of a fused silica wafer. (c) A uniform photoresist layer is formed on top of Cr by spin-coating. (d) The wafer and photomask is aligned on a contact aligner and photoresist is exposed by UV light. (e) The exposed areas on the photoresist are removed in the development. (f) Mask patterns are transferred to the Cr film by Cr etching. (g) The fused silica wafer is etching by Ar and SF_6 mixed plasma to obtain required depth. (h) After removing the residual Cr, the binary phase mask is finalized. (i) 3D profile of the central area on the fabricated binary phase mask taken with Zygo NewView 7300.

by a laser direct writer Heidelberg DWL2000 (Figure S.3 (a)). Each pixel on the pattern is $12.9 \mu\text{m}$. Second, the fused silica wafer is deposited with a 200 nm thick Cr film (Figure S.3 (b)) after cleaning in piranha solution. The Cr film will serve as a hard mask in the subsequent steps. Third, the fused silica wafer with Cr is spin-coated with a uniform layer of photoresist AZ1505 to form a $0.6 \mu\text{m}$ layer to be used in photolithography (Figure S.3 (c)). The photomask and the wafer coated with photoresist is then aligned on a EVG 6200 contact aligner for UV exposure (Figure S.3 (d)). The exposed area on the photoresist becomes soluble to the developer and can be removed by developer AZ726 (Figure S.3 (e)). The design patterns are transferred to the photoresist. The opening areas on the Cr film are then removed by Cr etchant (Figure S.3 (f)), such that the mask patterns are transferred to Cr hard mask. Residual photoresist is removed completely by ultrasonic rinse in acetone. Finally, the binary phase mask is obtained by etching the fused silica with mixed Argon and SF_6 plasma (Figure S.3 (g)). The etching depth corresponds to π at design wavelength $\lambda_0 = 550 \text{ nm}$. Finally, the binary phase mask is produced, as shown in Figure S.3 (h). The 3D profile of the fabricated binary phase mask is measured on Zygo NewView 7300 in Figure S.3 (i).

Reproducibility

Hardware Table S.2 lists the major components for the setup.

Table S.1. AO simulation parameters.

	Shack-Hartmann AO	Curvature AO	High Resolution AO (Ours)
Phase Screen Pixel Size	1 μm		
Phase Screen Resolution	5120 \times 5120		
Sensor Pixel Size	5 μm		
Sensor Resolution	1024 \times 1024		
Corrector Pixel Size	5 μm (SLM); 160 μm (Deformable Mirrors)		
Corrector Resolution	1024 \times 1024 (SLM); 32 \times 32 (Deformable Mirrors)		
Center Wavelength	550 nm		
Illumination	Uniform		
Propagation Distance z	\		
Propagation Method	Direct Integration [Shen and Wang 2006]	(Neighboring Planes) 1 mm	(Mask-Sensor) 0.5 mm
Reconstruction Method	Centroid Tracking	Angular Spectrum [Goodman 2005]	Teague's Method [Teague 1983]
Bilateral Window Size	Warping Scheme		
Additional Parameters	20 \times 20		
	Lenslets Number 32 \times 32		
	Effective Focal Length 7 mm		
	Sub-aperture Size 160 μm		

Table S.2. Setup components.

Description	Qty.	Model	Manufacturer
Plasma light source	1	HPLS245	Thorlabs
Collimation adapter	1	COP5-A	Thorlabs
Cage system iris	1	CP20S	Thorlabs
1" longpass filter, cut-on 700 nm	1	FEL0700	Thorlabs
1" achromatic doublets $f = 200$ mm	2	AC254-200-A	Thorlabs
1" achromatic doublets $f = 150$ mm	1	AC254-150-A	Thorlabs
1" wire grid polarizer	1	WP25M-VIS	Thorlabs
2" linear polarizer	1	LPVISE200-A	Thorlabs
2" shortpass dichroic mirror	1	DMSP650L	Thorlabs
2" longpass dichroic mirror	1	DMLP650L	Thorlabs
2" beamsplitter cube	1	BS031	Thorlabs
XY linear translation stage	1	XYT1/M	Thorlabs
Mounting stage for warped plates	1	XYFM1/M	Thorlabs
1" long cage assembly rod	4	ER1	Thorlabs
1.5" long cage assembly rod	4	ER1.5	Thorlabs
Reflective phase-only SLM	1	PLUTO-2-VIS-014-C	Holoeye
Bare sensor of wavefront sensor	1	GS3-U3-15S5M-C	PointGrey
Camera body	1	EOS 70D	Canon
Camera macro lens	1	EF 100 mm f/2.8	Canon
Waveform generator	1	33500B Series	Keysight
Motorized stage	1	T-LSM100A	Zaber
8.6 mm \times 8.6 mm square iris at SLM	1	3D printed	

REFERENCES

- Joseph W Goodman. 2005. *Introduction to Fourier optics*. Roberts and Company Publishers.
- Richard H Hudgin. 1977. Wave-front reconstruction for compensated imaging. *JOSA A* 67, 3 (1977), 375–378.
- Andrei N Kolmogorov. 1941. The local structure of turbulence in incompressible viscous fluid for very large Reynolds numbers. In *Dokl. Akad. Nauk SSSR*, Vol. 30. JSTOR, 301–305.
- RG Lane, A Glindemann, JC Dainty, et al. 1992. Simulation of a Kolmogorov phase screen. *Waves in random media* 2, 3 (1992), 209–224.
- Robert J Noll. 1978. Phase estimates from slope-type wave-front sensors. *JOSA A* 68, 1 (1978), 139–140.
- Neal Parikh, Stephen P Boyd, et al. 2014. Proximal Algorithms. *Foundations and Trends in optimization* 1, 3 (2014), 127–239.
- Fabin Shen and Anbo Wang. 2006. Fast-Fourier-transform based numerical integration method for the Rayleigh-Sommerfeld diffraction formula. *Appl. Opt.* 45, 6 (2006), 1102–1110.
- Michael Reed Teague. 1983. Deterministic phase retrieval: a Green's function solution. *JOSA A* 73, 11 (1983), 1434–1441.

Software Please refer to <https://github.com/vccimaging/MegapixelAO> for our open source repository.